The Astrophysical Journal, 988:277 (8pp), 2025 August 1 https://doi.org/10.3847/1538-4357/ade70b
© 2025. The Author(s). Published by the American Astronomical Society.
OPEN ACCESS

H I Absorption Line and Anomalous Dispersion in the Radio Pulses of PSR B1937+21

Jinchen Jiang (姜金辰)[1,2], Shunshun Cao (曹顺顺)[2,3], Kejia Lee (李柯伽)[1,2,4], Bojun Wang (王铂钧)[1], Heng Xu (胥恒)[1], Siyuan Chen[5], Yanjun Guo (郭彦君)[1,6], Peng Jiang (姜鹏)[1,7], Weicong Jing (景威聪)[1], Jiguang Lu (卢吉光)[1,7], Jiangwei Xu (徐江伟)[1], Renxin Xu (徐仁新)[2,3,4], and Zihan Xue (薛子涵)[2,4]
[1] National Astronomical Observatories, Chinese Academy of Sciences, Beijing 100101, People's Republic of China; jiangjinchen@pku.edu.cn, kjlee@pku.edu.cn
[2] Department of Astronomy, Peking University, Beijing 100871, People's Republic of China; r.x.xu@pku.edu.cn
[3] State Key Laboratory of Nuclear Physics and Technology, Peking University, Beijing 100871, People's Republic of China
[4] Kavli Institute for Astronomy and Astrophysics, Peking University, Beijing 100871, People's Republic of China
[5] Shanghai Astronomical Observatory, Chinese Academy of Sciences, Shanghai 200030, People's Republic of China
[6] Key Laboratory of Radio Astronomy and Technology, Chinese Academy of Sciences, Beijing 100101, People's Republic of China
[7] Guizhou Radio Astronomical Observatory, Guizhou University, Guiyang 550000, People's Republic of China
Received 2025 February 27; revised 2025 June 20; accepted 2025 June 21; published 2025 July 30

Abstract

We use the Five-hundred-meter Aperture Spherical radio Telescope to observe the bright millisecond pulsar PSR B1937+21 (J1939+2134) and record the data in the band from 1.0 to 1.5 GHz. We measure the neutral hydrogen (H I) emission and absorption lines near 1420 MHz ($\lambda \simeq 21$ cm). We derive the kinematic distance of the pulsar with the H I observation. By comparing this with the archival absorption spectra observed decades ago, we notice possible variations in the absorption spectra toward this pulsar, which correspond to a possible tiny-scale atomic structure of a few astronomical units in size. We also verify the apparent faster-than-light anomalous dispersion at the H I absorption line of this pulsar previously reported.

Unified Astronomy Thesaurus concepts: Radio pulsars (1353); Radio spectroscopy (1359); Pulsar timing method (1305); H I line emission (690); Neutral hydrogen clouds (1099)

1. Introduction

The interaction of the magnetic moments of the electron and proton is at the energy level of μeV, which leads to the "hyperfine splitting" of the energy level between the hydrogen atom "triplet" and "singlet" states. The energy of the triplet state is higher than the singlet state by approximately 6 μeV, i.e., 1420.4 MHz. H. C. van de Hulst (1945) predicted the 21 cm emission from neutral hydrogen (H I) in the space, which was later detected in 1951 (H. I. Ewen & E. M. Purcell 1951; C. A. Muller & J. H. Oort 1951). In the astronomical context, the H I absorption line was detected a few years later (J. P. Hagen & E. F. McClain 1954; J. P. Hagen et al. 1954; D. R. W. Williams & R. D. Davies 1954). It was immediately proposed that the radial velocity of emission and absorption lines, combined with the Galactic rotation curve, can be used to measure the distance of radio sources (D. R. W. Williams & R. D. Davies 1954), which is known as the H I kinematic distance. J. Gomez-Gonzalez & M. Guelin (1974) and D. A. Graham et al. (1974) first applied this method to the determination of pulsar distance. This method measures the distances of the emitting H I clouds in the background and the absorbing ones in the foreground, thus constraining the distance of a pulsar between the nearest background and farthest foreground clouds. Several surveys using this method have been published (see J. P. W. Verbiest et al. 2012 for a summary).

Beyond distance measurement, H I observations of pulsars help to resolve interstellar medium (ISM) fluctuations. The angular fluctuations in the H I absorption spectra were first discovered in the very long baseline interferometry (VLBI) observation of the extragalactic source 3C 147 (N. H. Dieter et al. 1976), which reflects tiny-scale atomic structure (TSAS; S. Stanimirović & E. G. Zweibel 2018) in the H I atoms of the ISM. The temporal variations in the H I absorption spectra toward pulsars can also be used to detect TSAS, which was noticed by T. R. Clifton et al. (1988) in the absorption spectra of PSR B1821+05. Several surveys were dedicated to the temporal variation of the H I absorption line toward pulsars using the Arecibo Telescope (D. A. Frail et al. 1994; S. Stanimirović et al. 2003, 2010; J. M. Weisberg & S. Stanimirović 2007), the Murriyang Telescope at Parkes Observatory (S. Johnston et al. 2003), and the Green Bank Telescope (GBT; A. H. Minter et al. 2005).

The H I energy level also affects the timing of pulsar radio signal around the transition frequency due to the electromagnetic wave propagation, as inferred from the Kramers–Kronig relation (e.g., J. D. Jackson 1998). The group velocity of electromagnetic wave propagating in the medium is

$$v_g = \frac{d\omega}{dk} = \frac{c}{n(\omega) + \omega \frac{dn}{d\omega}}, \quad (1)$$

where ω is the angular frequency of the wave, $n = ck/\omega$ is the refractive index of the medium, and c is the speed of light in vacuum (J. D. Jackson 1998). In most cases, v_g is slower than c. However, around absorption lines, the group velocity can be faster than c, if $dn/d\omega$ is sufficiently negative, i.e., in the strong anomalous dispersion regime (C. G. Garrett & D. E. McCumber 1970; J. D. Jackson 1998). It is worth noting that the superluminal propagation (group velocity) around absorption lines does not violate causality. When it happens, the leading edge of a pulse is less attenuated than the trailing edge, thus the peak which defines the group velocity

Original content from this work may be used under the terms of the Creative Commons Attribution 4.0 licence. Any further distribution of this work must maintain attribution to the author(s) and the title of the work, journal citation and DOI.

moves faster than the leading edge (J. D. Jackson 1998). The wide-band and periodic pulses from pulsars can be used to directly measure such anomalous dispersion of electromagnetic waves in the ISM. Indeed, 15 yr ago, the pioneer work (F. A. Jenet et al. 2010) detected such a "faster-than-light" propagation phenomenon around the H I frequency in the Arecibo data of PSR B1937+21 (J1939+2134). To detect such a phenomenon, one requires radio telescopes of great sensitivity that can accurately measure the time of arrivals in a rather narrow bandwidth of ∼100 kHz.

The Five-hundred-meter Aperture Spherical radio Telescope (FAST) concluded its commissioning and started science observation in 2020 (P. Jiang et al. 2019, 2020; L. Qian et al. 2020). As the largest and most sensitive radio telescope in the L-band (frequency around 1.4 GHz), FAST is capable of measuring the H I absorption line and anomalous dispersion accurately. In fact, such an experiment was proposed during the commissioning (J. Lu et al. 2020). Recently, W. C. Jing et al. (2023) constrained the H I kinematic distance of PSR B0458+46 using the spectral line backend of FAST.

In this paper, we focus on PSR B1937+21 (J1939+2134), the first millisecond pulsar ever discovered (D. C. Backer et al. 1982). Shortly after the discovery, C. Heiles et al. (1983) obtained its H I absorption spectrum and kinematic distance using the Arecibo Telescope. Though the kinematic distance is often less accurate compared with annual parallax measurement using pulsar timing or VLBI, it can estimate the distance of a pulsar in a single observation. The most recent astrometric result of PSR B1937+21 derives a parallax distance $2.9^{+0.3}_{-0.2}$ kpc (H. Ding et al. 2023). The dispersion measures (DMs) of pulsars can also be used to estimate their distances. With DM = 71 cm^{-3} pc for PSR B1937+21, the NE2001 model (J. M. Cordes & T. J. W. Lazio 2002; S. K. Ocker & J. M. Cordes 2024) estimates its distance at 3.6 kpc, while the estimation of the YMW16 model (J. M. Yao et al. 2017) is 2.9 kpc. We repeat the measurement of anomalous dispersion at the H I absorption line by F. A. Jenet et al. (2010). We also notice the variations in the H I absorption spectrum of PSR B1937+21 in Arecibo and FAST observations, which may be caused by a possible TSAS.

Section 2 describes the baseband observation of PSR B1937+21 using FAST. We obtain the H I emission and absorption spectra in Section 3.1, and decompose the spectra into Gaussian components in Section 3.2 to derive the kinematic distance of PSR B1937+21 in Section 3.3. The results are presented in Section 4. We compare the results with previous literature in Section 5, and the possible TSAS is discussed in Section 5.1.

2. Observation

The baseband data were recorded during a FAST observation of PSR B1937+21 (J1939+2134) on 2020 November 12 (MJD 59165). The observation was carried out within the small zenith angle range of FAST ($<26.^{\circ}4$) to optimize sensitivity and polarimetry accuracy. The observation length was 1 hr. We used the central beam of the L-band 19-beam receiver of FAST to track the pulsar at R.A. = $19^{\mathrm{h}}39^{\mathrm{m}}38^{\mathrm{s}}.56$, decl.=+21°34′59.″1 (J2000), or Galactic coordinates $l = 57^{\circ}30'32.''0$ and $b = -0^{\circ}17'22.''5$. The half-power beam width (HPBW) is 2.′82 at 1420 MHz (P. Jiang et al. 2020). The baseband signals of dual polarizations were sampled and recorded with a ROACH-2 based digital backend (P. Jiang et al. 2019), which sampled at the rate of 10^9 samples per second. The recorded signal covered 500 MHz observing bandwidth according to Nyquist sampling theorem, i.e., 1–1.5 GHz. The backend also simultaneously recorded filterbank data in the search-mode `PSRFITS` format (A. W. Hotan et al. 2004) with 4 coherency matrix elements (AABBCRCI), 4096 frequency channels, and a sampling time of 49.152 μs. The gain difference between the two polarizations is calibrated with the modulated noise calibrator signal from the noise diode. The noise signal was injected for 2 minutes before and after the observation.

3. Data Reduction and Analysis

3.1. Channelization, Folding, and Calibration

We use DSPSR (W. van Straten & M. Bailes 2011) to channelize and fold the baseband data off-line. We divide the 500 MHz bandwidth into 32,768 frequency channels, therefore the frequency resolution is 15.26 kHz/chan and the Nyquist time resolution is 65.536 μs. The dynamic spectrum is folded and interpolated into 1024 phase bins, in which the spin period in the pulsar ephemeris is updated by timing segments of our observation using TEMPO2 (G. B. Hobbs et al. 2006). We access the folded archive file with the PYTHON language interface of PSRCHIVE (A. W. Hotan et al. 2004). Thus, the dispersion delay between channels is removed with the PSRCHIVE, and the dispersion within the channel is coherently dedispersed with the DSPSR. The DM has been updated to 71.014527 ± 0.000006 cm^{-3} pc referencing to the Barycentric Coordinate Time (TCB) by aligning the short structures in giant pulses following the `DM_phase` algorithm (D. Michilli et al. 2018; A. Seymour et al. 2019). Polarization calibration is also performed using the PSRCHIVE.

We estimate the antenna temperature by comparing the off-pulse spectral baseline with the system temperature, then the flux density is derived using the antenna gain. The system temperature and aperture efficiency are interpolated to the zenith angle in the middle of the observation using the parameters in P. Jiang et al. (2020). We note that the H I emission in the beam may affect the measurement of the injected calibrator signal of the noise diode. Therefore, the calibration parameters around the H I emission line are interpolated using the parameters at neighboring frequencies.

3.2. Spectral Line Decomposition

The H I gas in the antenna beam contributes to the emission lines in both on- and off-pulse spectra, while only the H I gas in the foreground of the pulsar absorbs the pulsar emission at 21 cm. The H I spectral line is shifted in central frequency by the radial Doppler effect of the gas and broadened by the turbulent and thermal motion of the gas. By fitting the emission and absorption components one can derive the kinematic distance of the H I gas (Section 3.3) and reveal the connection between absorption and anomalous dispersion (Section 3.4).

The selected on- and off-pulse phase ranges are illustrated Figure 1, where the phase ranges with less than 1% and above 3% peak flux are manually selected as the off- and on-pulse regions, respectively. The off-pulse spectrum, which is derived by averaging over the off-pulse phases, consists of the system noise and H I emission line. The on-pulse spectrum consists of

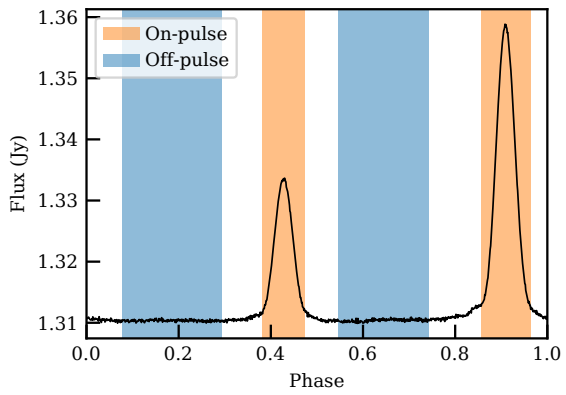


Figure 1. Integrated pulsar profile of PSR B1937+21. The baseband signal at 1–1.5 GHz is filtered into 32,768 frequency channels and folded into 1024 phase bins. The on-pulse (orange) and off-pulse (blue) ranges are visually selected.

the system noise, H I emission line, and pulsar signal with H I absorption. Therefore, we compute the pulsar spectrum with H I absorption with the on-off spectral subtraction.

As shown in Figure 2, there are multiple components in the emission and absorption spectra. In order to measure the radial velocity center and scattering of each H I cloud (clumps of H I gas), it is necessary to decompose the spectra. Using the χ^2 test, we note that six Gaussian components, together with a constant spectrum baseline, are enough to model the observed spectrum. Our fitting model is

$$T_{\rm A}(f) = A_0 + \sum_{i=1}^{6} A_i e^{-\frac{(f-f_{c,i})^2}{2f_{d,i}^2}}, \tag{2}$$

where A_0 is the constant baseline, and A_i, $f_{c,i}$, and $f_{d,i}$ are the amplitude, center, and half-width of the ith Gaussian components, respectively.

The observed pulsar spectrum is affected by ISM scintillation. As an example, the Arecibo observation of PSR B0540 +23 and B2016+28 showed significant scintillation ripples in the pulsar spectra (S. Stanimirović et al. 2010). In our observation, the broadband pulsar spectrum is bright around 1420 MHz and fades as the frequency increases. Thus, the H I absorption lines occur on the slope of the pulsar spectrum. The scintillation ripples should be carefully removed before measuring absorptive components, otherwise they may generate false structures in the absorption spectra. We use the 1D spline with explicit internal knots `LSQUnivariateSpline` in `SciPy` (P. Virtanen et al. 2020) to fit for the baseline and interpolate around the absorption lines. For the absorption spectrum, four Gaussian components are enough to fit the optical depth, i.e., the optical depth is

$$S/S_b = \exp\left[-\sum_{i=1}^{4} A_i \exp\left(-\frac{(f-f_{c,i})^2}{2f_{d,i}^2}\right)\right], \tag{3}$$

where S is the pulsar spectrum and S_b is the baseline.

All the spectral model parameters are inferred with the standard curve-fitting Bayesian method. The sampling of posterior is performed using MULTINEST (F. Feroz & M. P. Hobson 2008; F. Feroz et al. 2009) and PYMULTINEST(J. Buchner 2016). We adopt maximum posterior estimator as the central value of our models.

3.3. H I Kinematic Distance of the Pulsar

The kinematic distance is determined based on the radial velocity of the source and the general revolution of the the Milky Way. If the source follows the circular orbit of the Galaxy in a certain direction, its radial velocity will depend on its distance according to the Galactic rotation curve. Therefore, by measuring the radial velocity of the source, it is possible to determine its distance. Following M. Fich et al. (1989), the observed radial velocity of the source should be

$$v_r = R_0(\omega - \omega_0)\sin l \cos b, \tag{4}$$

where R_0 is the solar distance to the Galactic center, l and b are the Galactic coordinates of the source, and ω and ω_0 are the angular velocity of the source and the solar system, respectively. Equation (4) is related to the distances to the Galactic center of the source R and of the Sun R_0 by

$$\Theta_0 = \omega R = \omega_0 R_0, \tag{5}$$

and is related to the distance d between them by

$$R^2 = R_0^2 + d^2 - 2R_0 d\cos l, \tag{6}$$

where Θ_0 is the circular rotation speed of the Milky Way. Combining Equations (4)–(6), the kinematic distance of the source is[8]

$$d = R_0\left[\cos l \pm \sqrt{\left(1 + \frac{v_r}{\Theta_0 \sin l \cos b}\right)^{-2} - \sin^2 l}\right]. \tag{7}$$

For the outer Galaxy ($\cos l < 0$), it is easy to exclude a negative root. However, for the inner Galaxy ($\cos l > 0$), the near and far roots on either sides of the tangent point are both possible, which is known as kinematic distance ambiguity (J. S. Urquhart et al. 2012).

When applying this method to pulsars, the procedure is complicated due to lack of spectral lines in the pulsar radiation. The observer can only measure the spectral lines of foreground and background clouds to constrain the pulsar distance. For foreground clouds, the observer detects the emission line from the clouds and the absorption line in the pulsar emission. For background clouds, only emission lines can be detected. Thus the pulsar distance is constrained between the farthest absorptive cloud and the nearest emission-only cloud.

In this work, we adopt the distance to the Galactic center $R_0 = 8.34$ kpc and the circular rotation speed $\Theta_0 = 240\,{\rm km\,s^{-1}}$ at the Sun (M. J. Reid et al. 2014). The rotation speed is measured in the local standard of rest (LSR), in which the barycentric velocity is $(U, V, W)_\odot = (11.1, 12.24, 7.25)\,{\rm km\,s^{-1}}$ defined in Galactic Cartesian velocity components (R. Schönrich et al. 2010). These updated values are slightly different from the current International Astronomical Union (IAU) standard $\Theta_0 = 220\,{\rm km\,s^{-1}}$, $R_0 = 8.5$ kpc, and $(U, V, W)_\odot = (10.0, 15.4, 7.8)\,{\rm km\,s^{-1}}$ (F. J. Kerr & D. Lynden-Bell 1986). The choice of the above galactic model parameters introduce negligible effects compared to the systematics of kinematic distance method (about $2\,{\rm km\,s^{-1}}$ in radial velocity and about 1 kpc or less in kinematic distances).

The topocentric frequency of the H I spectrum is first corrected to the barycenter of the solar system. Then the barycentric radial velocity of H I emission and absorption lines are derived from their frequency difference from the reference

[8] Equation (2) in J. M. Weisberg et al. (2008) was mistyped.

frequency 1420.4057517667 MHz measured in the laboratory (G. W. F. Drake 2006). The radial velocity in the LSR, $v_{\rm LSR}$, is then obtained by adding the projection toward the source of $(U, V, W)_\odot$. An uncertainty of $\pm 7\,{\rm km\,s^{-1}}$ is added to the radial velocity due to the streaming and random motion of the clouds in the Galaxy (D. A. Frail & J. M. Weisberg 1990; J. M. Weisberg et al. 2008). The kinematic distance of the pulsar is derived from the off-pulse emission spectrum and the on-pulse absorption spectrum. The pulsar distance must be larger than all absorption components' distances in the on-pulse absorption spectrum, and probably smaller than the distances of the components that only exist in the off-pulse emission spectrum.

3.4. Timing and the Anomalous Dispersion

We use pulsar-timing techniques to measure the pulse time of arrival at each frequency (D. R. Lorimer & M. Kramer 2005). The timing template is averaged between 1415 and 1425 MHz and smoothed, with the frequencies of the H I line excluded. We implement the Fourier phase gradient algorithm (J. H. Taylor 1992) to time the integrated pulse profiles around the H I absorption line with a `Python` script.

The timing results are used as independent data to validate our absorption spectrum measurement. As mentioned in Section 3.2, ISM scintillation may generate ripples in the absorption spectra. In addition, J. M. Weisberg et al. (1980) and S. Stanimirović et al. (2010) pointed out that the small number of voltage levels in the digital spectrometer can generate large digitization errors and "ghost" in the spectrum. The noise temperature may also increase significantly due to bright H I emission, which decreases the signal-to-noise ratio (S/N) in the absorption spectrum (S. Johnston et al. 2003). While the spectral measurement is vulnerable to artifacts due to ISM and instrumental effects, the pulsar timing is less affected. According to the Kramers–Kronig relations (causality of the Green's function), dispersion must arise when resonance radiation or absorption occurs (J. D. Jackson 1998). The Lorentz dispersion model is a classical model that considers electrons in the medium as the damped harmonic oscillators. We follow F. A. Jenet et al. (2010) to assume that the radial velocity distribution of each H I cloud is Gaussian, i.e., the H I optical depth $\tau(f) = \tau_0 \exp\left[-\frac{(f-f_c)^2}{2f_d^2}\right]$. In Equation (16) of F. A. Jenet et al. (2010), the dispersion delay Δ is related to the optical depth amplitude τ_0 and line width f_d in the absorption profile by[9]

$$\begin{aligned}\Delta(f) &= \frac{\tau_0}{2\sqrt{2}\,\pi f_d}\left[\frac{f-f_c}{\sqrt{2}f_d}\,{\rm Im}\,w\left(\frac{f-f_c}{\sqrt{2}f_d}\right) - \frac{1}{\sqrt{\pi}}\right] \\ &= \frac{\tau_0}{2\sqrt{2}\,\pi f_d}\left[\frac{f-f_c}{\sqrt{2}f_d}\exp\left(-\frac{(f-f_c)^2}{2f_d^2}\right){\rm erfi}\left(\frac{f-f_c}{\sqrt{2}f_d}\right) - \frac{1}{\sqrt{\pi}}\right],\end{aligned} \tag{8}$$

where the Faddeeva function $w(z) = \exp(-z^2){\rm erfc}(-iz) = \frac{i}{\pi}\int_{-\infty}^{+\infty}\frac{e^{-t^2}}{z-t}dt$ (M. Abramowitz & I. A. Stegun 1972), and the imaginary error function ${\rm erfi}(x) = \frac{2}{\sqrt{\pi}}\int_0^x e^{t^2}dt$. $\Delta(f)$ reaches first at the line center where $\Delta_c = -\frac{\tau_0}{(2\pi)^{3/2}f_d}$, which depends on the column density of the H I cloud and the velocity dispersion inside it. According to Equation (8), the anomalous dispersion is sensitive to narrow and deep absorptive features in the spectrum. In this way, we can infer the absorption spectra from the dispersion delay.

[9] A factor $\sqrt{2}$ is missing in Equation (16) in F. A. Jenet et al. (2010).

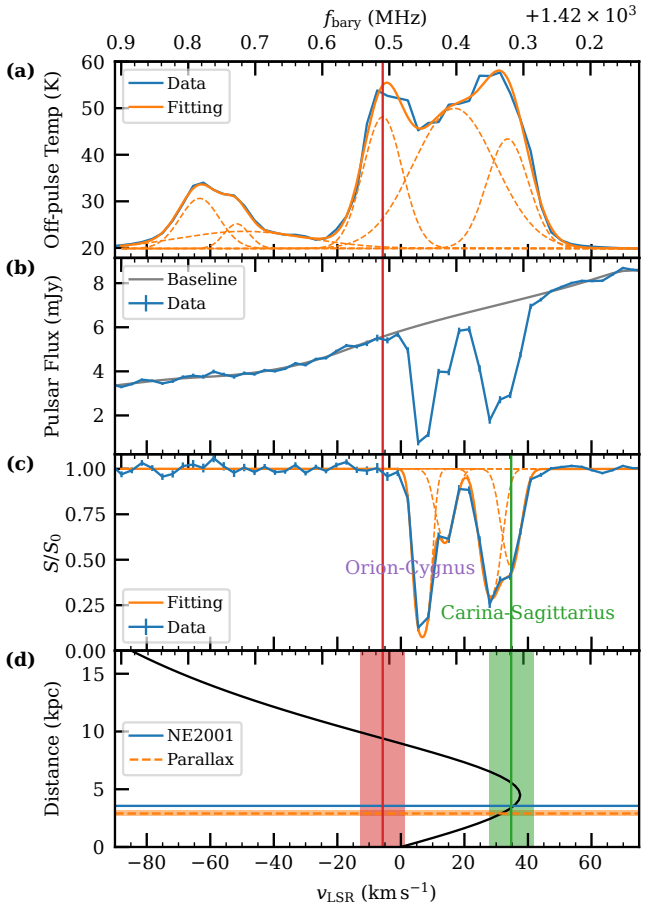


Figure 2. Kinematic distance of PSR B1937+21. The upper x-axis is the barycentric frequency of the spectra. The lower x-axis is the radial velocity in the local standard of rest (LSR). (a) The emission spectrum of antenna temperature at off-pulse phases. The observed spectrum (blue) is fitted with six Gaussian components and a constant baseline. The components are plotted with orange dashed curves, and their summation is plotted with the orange solid curve. (b) The absorption spectrum of pulsar emission. The observed spectrum is marked in blue. The gray curve shows the fitted baseline. (c) The absorbed fraction. The blue curve is the observed absorption spectrum divided by the baseline in panel (b). The fitted Gaussian components are plotted with orange dashed lines, and the total absorption is plotted with the orange solid line. (d) The radial velocity of Galactic rotation as a function of distance at the direction of PSR B1937+21. The vertical red line denotes the radial velocity of the fourth Gaussian component in the emission spectrum and the red shade denotes its $\pm 7\,{\rm km\,m^{-1}}$ error, which determines the upper bound of the kinematic distance in the Perseus Arm. The vertical green line denotes the radial velocity of the fourth Gaussian component in the absorption spectrum and the green shade denotes its $\pm 7\,{\rm km\,m^{-1}}$ error, which determines the lower bound of the kinematic distance in the Carina–Sagittarius Arm. The horizontal blue line is the DM distance estimated using the YMW16 model (J. M. Yao et al. 2017). The horizontal orange dashed line is the distance calculated from the VLBI parallax (H. Ding et al. 2023).

4. Results

4.1. Spectral Line Decomposition and Kinematic Distance

The off-pulse emission spectrum is decomposed into six Gaussian components and a constant baseline as shown in panel (a) of Figure 2. The fitted parameters of the components

Table 1
Decomposition of the Emission Lines

Component	A (K)	f_c (MHz)	f_d (MHz)	$v_{\rm LSR}$ (km s^{-1})	Galactic Arm
Gaussian 1	$23.5\ ^{+6.0}_{-0.6}$	$1420.3234\ ^{+0.0050}_{-0.0008}$	$0.03096\ ^{+0.00400}_{-0.00014}$	$33.62\ ^{+0.17}_{-1.00}$	Carina–Sagittarius
Gaussian 2	$30.10\ ^{+0.26}_{-2.20}$	$1420.4028\ ^{+0.0120}_{-0.0034}$	$0.0611\ ^{+0.0015}_{-0.0090}$	$16.9\ ^{+0.7}_{-2.5}$	local/Carina–Sagittarius/Perseus
Gaussian 3	$28.3\ ^{+2.4}_{-1.7}$	$1420.5099\ ^{+0.0007}_{-0.0030}$	$0.0291\ ^{+0.0022}_{-0.0010}$	$-5.72\ ^{+0.60}_{-0.15}$	Perseus
Gaussian 4	3.7 ± 0.7	$1420.717\ ^{+0.013}_{-0.017}$	$0.095\ ^{+0.020}_{-0.006}$	$-49.4\ ^{+4.0}_{-2.8}$	Outer
Gaussian 5	$5.3\ ^{+1.6}_{-0.9}$	$1420.728\ ^{+0.006}_{-0.005}$	$0.0186\ ^{+0.0050}_{-0.0030}$	$-51.7\ ^{+1.0}_{-1.2}$	Outer
Gaussian 6	10.8 ± 0.8	1420.783 ± 0.004	$0.0294\ ^{+0.0025}_{-0.0040}$	-63.3 ± 0.9	Outer
Baseline	$19.865\ ^{+0.031}_{-0.100}$				

Note. The fitting model is defined in Equation (2). The frequencies are in the LSR.

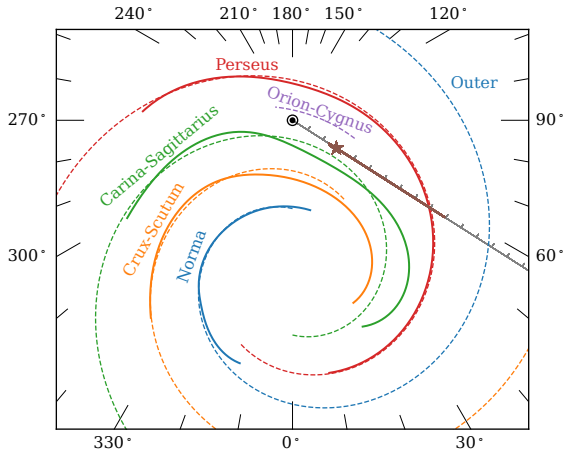


Figure 3. Distance measurement of PSR B1937+21 in the the Milky Way. The galactic arms are denoted with different colors, viz. Norma–Outer Arm (blue), Crux–Scutum Arm (orange), Carina–Sagittarius Arm (green), Perseus Arm (red), and the local Orion–Cygnus Arm (purple). The solid curves represent the Galactic arm model by J. H. Taylor & J. M. Cordes (1993), while the dashed curves represents the model by R. J. Wainscoat et al. (1992). The circle-dot represents the Sun. The gray dashed line shows the line of sight toward PSR B1937+21, with knots separated by 1 kpc. The brown solid line denotes the kinematic distance of the pulsar derived in this article, and the brown star represents its parallax distance $2.9^{+0.3}_{-0.2}$ kpc (H. Ding et al. 2023).

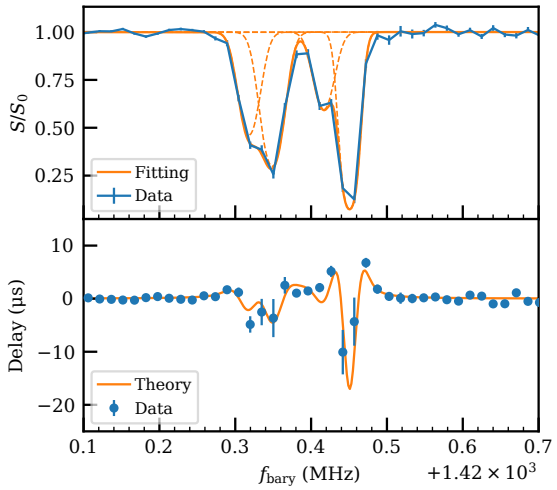


Figure 4. Anomalous dispersion around the H I absorption line in the emission of PSR B1937+21. The upper panel is identical to panel (c) in Figure 2. The lower panel shows the dispersion delay of the pulses, in which the blue dots are measured TOAs, and the orange curve is the theoretical result derived from the absorption spectrum using Equation (8).

are presented in Table 1. According to Figures 2 and 3, and Figure 3 of M. J. Reid et al. (2019), we attribute three emission components (Gaussian 4, 5, and 6 in Table 1) around $v_{\rm LSR} = -60\,{\rm km\,s^{-1}}$ to the Outer Arm of the the Milky Way, the component around $-5\,{\rm km\,s^{-1}}$ (Gaussian 3 in Table 1) to the Perseus Arm, and the component around $35\,{\rm km\,s^{-1}}$ (Gaussian 1 in Table 1) to the Carina–Sagittarius Arm. The wide Gaussian component 2 in Table 1 may consist of the contribution from the local Orion–Cygnus Arm, Carina–Sagittarius Arm, and Perseus Arm.

The baseline in the pulsar spectrum is fitted as shown in panel (b) of Figure 2. After removing the baseline due to ISM scintillation, we identify four absorption components in the spectrum as shown in panel (c) of Figure 2. We attribute Gaussian components 3 and 4 to the local Orion–Cygnus Arm, and Gaussian components 1 and 2 to Carina–Sagittarius Arm.

The lower bound of the kinematic distance is derived from Gaussian component 4 in Table 2 at $v_{\rm LSR} \approx 35\,{\rm km\,s^{-1}}$. This component is close to the tangent point in Carina–Sagittarius Arm, which is within the $7\,{\rm km\,s^{-1}}$ error range due to the streaming and random motion of the clouds. Therefore, we adopt the both larger and smaller solutions in Equation (7) for a $7\,{\rm km\,s^{-1}}$ error as the uncertainty of the lower bound of kinematic distance, which is determined at $D_L = 4.5 \pm 2.1$ kpc.

The upper bound of the kinematic distance is derived from Gaussian component 4 in Table 1 at $v_{\rm LSR} \approx -5\,{\rm km\,s^{-1}}$, where no absorption line can be identified. Considering a $7\,{\rm km\,s^{-1}}$ error due to the streaming and random motion of the clouds, the upper bound of the kinematic distance is $D_U = 9.4 \pm 0.5$ kpc according to Equation (7).

4.2. Anomalous Dispersion

The lower panel in Figure 4 exhibits the measured times of arrival (TOAs) around the H I absorption line in the pulsar emission. At the center of the fourth absorption component, the dispersion delay reaches $-10\,\mu$s, i.e., the pulse is faster than light by about $10\,\mu$s. With the Gaussian decomposition of the absorption spectrum in the upper panel of Figure 4, we derive the theoretical delay curve in the lower panel from Equation (8), which matches well with the observed TOAs.

Table 2
Decomposition of the Absorption Lines

Component	A	f_c (MHz)	f_d (MHz)	$v_{\rm LSR}$ (km s^{-1})	Galactic Arm
Gaussian 1	$0.77^{+0.09}_{-0.08}$	$1420.3182^{+0.0034}_{-0.0025}$	$0.0127^{+0.0021}_{-0.0015}$	$34.7^{+0.5}_{-0.7}$	Carina–Sagittarius
Gaussian 2	$1.21^{+0.09}_{-0.11}$	$1420.3488^{+0.0021}_{-0.0017}$	$0.0132^{+0.0013}_{-0.0015}$	$28.3^{+0.4}_{-0.5}$	Carina–Sagittarius
Gaussian 3	0.52 ± 0.04	$1420.4167^{+0.0014}_{-0.0013}$	$0.0125^{+0.0017}_{-0.0013}$	$13.94^{+0.26}_{-0.30}$	local
Gaussian 4	2.60 ± 0.17	1420.4508 ± 0.0006	0.0093 ± 0.0004	6.75 ± 0.12	local

Note. The fitting model is defined in Equation (3). The frequencies are in the LSR.

5. Discussion

5.1. A Possible Tiny-scale Atomic Structure

PSR B1937+21 is associated with the continuum radio source 4C 21.53W, which is a slightly extended H II region (W. Sieber & J. H. Seiradakis 1984). In the vicinity, 4C 21.53E (1938+215) is an extragalactic double source (W. C. Erickson 1983). The supernova remnant (SNR) G57.2+0.8 (1932+218) is also known as 4C 21.53 (S. Ranasinghe et al. 2018; W. D. Cotton et al. 2024), which is the host of magnetar SGR J1935+2154 and is not related to PSR B1937+21.

The absorption lines in the pulsar spectra of PSR B1937+21 were previously measured by C. Heiles et al. (1983) and F. A. Jenet et al. (2010) using the Arecibo Telescope. Figure 1 of C. Heiles et al. (1983) presented a narrow absorption feature at $-10\,{\rm km\,s^{-1}}$ in the absorption spectra toward PSR B1937+21 and 4C 21.53W, which was suspected to be absorbed by a nearby small dust cloud. This narrow absorption line disappeared in the absorption spectrum toward this pulsar, as shown in Figure 2 of F. A. Jenet et al. (2010) and in Figure 2 of this article. We also notice that a wider and shallower component connected the $-10\,{\rm km\,s^{-1}}$ component to the $+10\,{\rm km\,s^{-1}}$ component in the absorption spectra in C. Heiles et al. (1983) and F. A. Jenet et al. (2010), which is also missing in our result. The comparison of the three absorption spectra is presented in Figure 5.

If the observed variation in the H I absorption spectrum is caused by transverse motion of H I cloud across the line of sight (LoS) toward the pulsar, the transverse size of the H I cloud can be roughly estimated. The transverse size of the cloud can be derived from the variation timescale of H I absorption line and the transverse velocity of the cloud relative to the LoS. However, our knowledge of both factors is very limited. The H I absorption spectrum of PSR B1937+21 was only measured in three epochs separated by decades, which can only poorly imply the variation timescale. The proper motion and distance of the cloud are also unknown. Following previous studies such as A. H. Minter et al. (2005), we estimate the transverse speed by multiplying the proper motion of PSR B1937+21 with half of its distance. We must point out the large uncertainty in this estimation. With the proper motion $0.24\,{\rm mas\,yr^{-1}}$ and the distance $D = 1/\varpi = 1/(0.34\,{\rm mas}) = 2.9\,{\rm kpc}$ of PSR B1937+21 (H. Ding et al. 2023), the variation between 1983 and 2009 corresponds to a spatial structure around 9 au at halfway toward the pulsar, and the variation between 2009 and 2020 corresponds to a structure around 4 au, assuming the H I cloud is at halfway toward the pulsar.

Temporal variations of H I absorption profiles toward pulsars have been reported for several pulsars, including PSR B1821+05 (T. R. Clifton et al. 1988; D. A. Frail et al. 1991), B1557−50 (A. A. Deshpande et al. 1992; S. Johnston et al. 2003), and B0301+19 (J. M. Weisberg et al. 2008). The variations are attributed to the TSASs in the ISM (S. Stanimirović & E. G. Zweibel 2018). The TSAS toward PSR B1937+21 has not been reported in previous literature. This detection provides a new source to monitor the tiny-scale fluctuation of H I in the ISM.

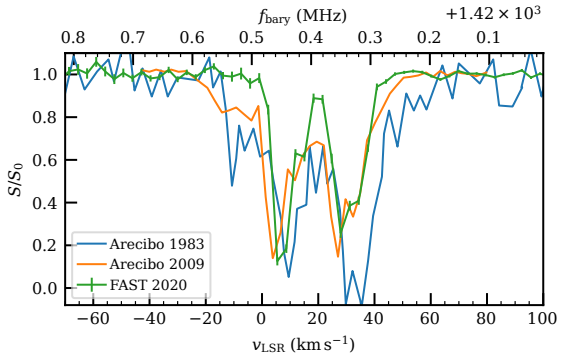


Figure 5. Temporal evolution of the H I absorption spectrum toward PSR B1937+21. The blue curve is the Arecibo result extracted from Figure 1 of C. Heiles et al. (1983). The orange curve is the Arecibo result extracted from Figure 3 of F. A. Jenet et al. (2010). A velocity offset $-20\,{\rm km\,s^{-1}}$ is applied to align its corresponding emission spectrum with the FAST emission spectrum, because the frequency in F. A. Jenet et al. (2010) was topocentric. The data points are digitized using `PlotDigitizer` (https://plotdigitizer.com/app). The green curve is the result of the current work.

However, we must emphasize that the measurement of H I absorption spectra is vulnerable to possible errors generated during observation and data reduction, as mentioned in Section 3.4. S. Johnston et al. (2003) pointed out the lack of significance contours manifesting the noise increase due to H I emission in the earlier study by D. A. Frail et al. (1994). J. M. Weisberg et al. (1980) and S. Stanimirović et al. (2010) noted that the limited number of voltage levels can generate large digitization errors and "ghost" in the spectrum. We also find that the pulsar spectrum of PSR B1937+21 shows strong scintillation ripples, as also noticed by S. Stanimirović et al. (2010). Therefore, the baseline removal is crucial in the H I absorption line measurement.

There are also possible variations in other absorption components. In the absorption spectrum in F. A. Jenet et al. (2010), the two prominent components at 1420.26 and 1420.37 MHz (topocentric frequency) showed similar amplitude. In our observation, the higher-frequency peak is deeper. The anomalous dispersion presented in Section 4.2 and Figure 4 may also provide evidence for the possible TSAS. Unlike the spectral line measurement, the digitization error and ISM scintillation should affect the errors of TOAs rather than their expectations. The dispersion delay observed in our observation (lower panel of Figure 4) is significantly different

from Figure 3 of F. A. Jenet et al. (2010), which implies that the absorption spectrum has also changed. Unfortunately, the dispersion delay was not measured in C. Heiles et al. (1983), and the dispersion is insensitive to the broad component around 1420.45 MHz (topocentric frequency) in F. A. Jenet et al. (2010); therefore the previously discussed TSAS around $v_{\rm LSR} = -5\,{\rm km\,s^{-1}}$ cannot be fully assured using anomalous dispersion.

5.2. Update of Kinematic Distance of PSR B1937+21

The kinematic distance of PSR B1937+21 has been measured in several previous studies. C. Heiles et al. (1983) acquired the H I emission and absorption spectra of PSR B1937+21 using the Arecibo Telescope shortly after its discovery (D. C. Backer et al. 1982). Their pulsar spectrum did not show as much absorption around $v_r = 40\,{\rm km\,s^{-1}}$ as the nearby H II region 4C 21.53W and extragalactic source 4C 21.53E. They concluded that the pulsar must be closer to us than the tangent point of the spiral arm, and therefore the pulsar distance should be smaller than 5 kpc. By contrast, D. A. Frail & J. M. Weisberg (1990) set the lower limit of pulsar distance $D_L = 4.9 \pm 1.9$ kpc at the tangent point, and moved the upper limit to $D_U = 14.8 \pm 0.9$ kpc with the H I emission line around $v_r = -60\,{\rm km\,s^{-1}}$.

In this paper, our lower bound of kinematic distance $D_L = 4.5 \pm 2.1$ kpc is similar to the result of D. A. Frail & J. M. Weisberg (1990) because we identify the same H I absorption component near the tangent point. However, we shorten the upper bound from 14.8 ± 0.9 kpc (D. A. Frail & J. M. Weisberg 1990) in the Outer Arm to 9.4 ± 0.5 kpc in the Perseus Arm, because we recognize that Gaussian component 3 around $-5\,{\rm km\,s^{-1}}$ in the emission spectrum has no counterpart in the absorption spectrum. We agree with C. Heiles et al. (1983) and D. A. Frail & J. M. Weisberg (1990) that the absorption at approximately -5 and $-10\,{\rm km\,s^{-1}}$ was caused by local cloud with noncircular motion. This argument can be supported by DM and parallax distances. Our result is consistent with the more accurate parallax distance $2.9^{+0.3}_{-0.2}$ kpc (H. Ding et al. 2023).

5.3. Anomalous Dispersion Measurement in Pulsar Observation

Our result confirms the pioneer discovery of apparent faster-than-light dispersion around the H I absorption line (F. A. Jenet et al. 2010), though the delay curve has changed since 2009 as discussed in Section 5.1. In the lower panel of Figure 4, the negative delay at the line center implies that the group velocity $v_{\rm g}$ is greater than the speed of light in vacuum. As discussed in Section 3.4, the superluminal group velocity at the center of absorption line can be derived from classical electrodynamics. However, it does not violate causality. The group velocity $v_{\rm g} = d\omega/dk$ is defined as the speed of the Gaussian peak of the wave packet (J. D. Jackson 1998). When radiation or absorption occurs, $v_{\rm g}$ is not the equivalent to the propagation speed of information (F. A. Jenet et al. 2010). The connection between absorption and dispersion, known as the Kramers–Kronig relation, is the result of causality in the Green's function of radio wave propagation in the medium (J. D. Jackson 1998).

According to Equation (8), the amplitude of anomalous dispersion depends on both the amplitude and the width of the absorption line. The measurement of anomalous dispersion is sensitive to deep and narrow absorption features. However, deep absorption also decreases the observed brightness, which decreases the S/N of the pulse profiles and increases the errors of TOAs. Therefore, the successful measurement of anomalous dispersion in pulsar emission requires dense H I clouds with small velocity dispersion, and bright pulsars in the background. PSR B1937+21 resides near the tangent point, from where the radio wave propagates through a long path in Carina–Sagittarius Arm and the local Orion–Cygnus Arm. The high flux of PSR B1937+21 also increases the precision of timing. We recommend bright millisecond pulsars around tangent points of spiral arms for observations in the future.

Acknowledgments

We thank the anonymous reviewer and Joel Weisberg for helpful comments. This work made use of the data from FAST (Five-hundred-meter Aperture Spherical radio Telescope) (https://cstr.cn/31116.02.FAST). FAST is a Chinese national mega-science facility, operated by National Astronomical Observatories, Chinese Academy of Sciences. J.J.C. thanks Pengfei Wang and Chao Wang at NAOC, CAS and Xun Shi at YNAO, CAS for inspiring discussions. This work is supported by the National SKA Program of China (2020SKA0120100), the National Natural Science Foundation of China (Nos. 12003047 and 12133003), and the Strategic Priority Research Program of the Chinese Academy of Sciences (No. XDB0550300). This work is also supported by the Chinese Academy of Sciences Project for Young Scientists in Basic Research, grant No. YSBR-063; National Science Foundation of China 12225303, 12421003; and Strategic Priority Research Program of the Chinese Academy of Sciences, grant No. XDA0350501.

Facility: FAST.

Software: DSPSR (W. van Straten & M. Bailes 2011). PSRCHIVE (A. W. Hotan et al. 2004), TEMPO2 (G. B. Hobbs et al. 2006), MultiNest (F. Feroz & M. P. Hobson 2008; F. Feroz et al. 2009), PyMultiNest (J. Buchner 2016), Astropy (Astropy Collaboration et al. 2013, 2018), Numpy (C. R. Harris et al. 2020), SciPy (P. Virtanen et al. 2020), Matplotlib (J. D. Hunter 2007), MWPROP (S. K. Ocker & J. M. Cordes 2024), PlotDigitizer (https://plotdigitizer.com/app).

ORCID iDs

Jinchen Jiang (姜金辰) https://orcid.org/0000-0002-6465-0091
Shunshun Cao (曹顺顺) https://orcid.org/0009-0007-3817-8188
Kejia Lee (李柯伽) https://orcid.org/0000-0002-1435-0883
Bojun Wang (王铂钧) https://orcid.org/0000-0002-9434-4773
Heng Xu (胥恒) https://orcid.org/0000-0002-5031-8098
Siyuan Chen https://orcid.org/0000-0002-3118-5963
Yanjun Guo (郭彦君) https://orcid.org/0009-0008-1501-273X
Weicong Jing (景威聪) https://orcid.org/0000-0002-1056-5895
Jiguang Lu (卢吉光) https://orcid.org/0000-0002-9815-5873
Jiangwei Xu (徐江伟) https://orcid.org/0009-0008-7805-091X
Renxin Xu (徐仁新) https://orcid.org/0000-0002-9042-3044
Zihan Xue (薛子涵) https://orcid.org/0009-0001-6555-3269

References

Abramowitz, M., & Stegun, I. A. 1972, Handbook of Mathematical Functions (New York: Dover), 297
Astropy Collaboration, Price-Whelan, A. M., Sipöcz, B. M., et al. 2018, AJ, 156, 123
Astropy Collaboration, Robitaille, T. P., Tollerud, E. J., et al. 2013, A&A, 558, A33
Backer, D. C., Kulkarni, S. R., Heiles, C., Davis, M. M., & Goss, W. M. 1982, Natur, 300, 615
Buchner, J., 2016 PyMultiNest: Python interface for MultiNest, Astrophysics Source Code Library, ascl:1606.005
Clifton, T. R., Frail, D. A., Kulkarni, S. R., & Weisberg, J. M. 1988, ApJ, 333, 332
Cordes, J. M., & Lazio, T. J. W. 2002, arXiv:astro-ph/0207156
Cotton, W. D., Kothes, R., Camilo, F., et al. 2024, ApJS, 270, 21
Deshpande, A. A., McCulloch, P. M., Radhakrishnan, V., & Anantharamaiah, K. R. 1992, MNRAS, 258, 19P
Dieter, N. H., Welch, W. J., & Romney, J. D. 1976, ApJL, 206, L113
Ding, H., Deller, A. T., Stappers, B. W., et al. 2023, MNRAS, 519, 4982
Drake, G. W. F. 2006, Springer Handbook of Atomic, Molecular, and Optical Physics, 177 (Berlin: Springer)
Erickson, W. C. 1983, ApJL, 264, L13
Ewen, H. I., & Purcell, E. M. 1951, Natur, 168, 356
Feroz, F., & Hobson, M. P. 2008, MNRAS, 384, 449
Feroz, F., Hobson, M. P., & Bridges, M. 2009, MNRAS, 398, 1601
Fich, M., Blitz, L., & Stark, A. A. 1989, ApJ, 342, 272
Frail, D. A., Cordes, J. M., Hankins, T. H., & Weisberg, J. M. 1991, ApJ, 382, 168
Frail, D. A., & Weisberg, J. M. 1990, AJ, 100, 743
Frail, D. A., Weisberg, J. M., Cordes, J. M., & Mathers, C. 1994, ApJ, 436, 144
Garrett, C. G., & McCumber, D. E. 1970, PhRvA, 1, 305
Gomez-Gonzalez, J., & Guelin, M. 1974, A&A, 32, 441
Graham, D. A., Mebold, U., Hesse, K. H., Hills, D. L., & Wielebinski, R. 1974, A&A, 37, 405
Hagen, J. P., & McClain, E. F. 1954, ApJ, 120, 368
Hagen, J. P., McClain, E. F., & Hepburn, N. 1954, AJ, 59, 323
Harris, C. R., Millman, K. J., van der Walt, S. J., et al. 2020, Natur, 585, 357
Heiles, C., Kulkarni, S. R., Stevens, M. A., et al. 1983, ApJL, 273, L75
Hobbs, G. B., Edwards, R. T., & Manchester, R. N. 2006, MNRAS, 369, 655
Hotan, A. W., van Straten, W., & Manchester, R. N. 2004, PASA, 21, 302
Hunter, J. D. 2007, CSE, 9, 90
Jackson, J. D. 1998, Classical Electrodynamics, 3rd Edition (Weinheim: Wiley-VCH)
Jenet, F. A., Fleckenstein, D., Ford, A., et al. 2010, ApJ, 710, 1718
Jiang, P., Tang, N.-Y., Hou, L.-G., et al. 2020, RAA, 20, 064
Jiang, P., Yue, Y., Gan, H., et al. 2019, SCPMA, 62, 959502
Jing, W. C., Han, J. L., Hong, T., et al. 2023, MNRAS, 523, 4949
Johnston, S., Koribalski, B., Wilson, W., & Walker, M. 2003, MNRAS, 341, 941
Kerr, F. J., & Lynden-Bell, D. 1986, MNRAS, 221, 1023
Lorimer, D. R., & Kramer, M. 2005, Handbook of Pulsar Astronomy, 4 (Cambridge: Cambridge Univ. Press)
Lu, J., Lee, K., & Xu, R. 2020, SCPMA, 63, 229531
Michilli, D., Seymour, A., Hessels, J. W. T., et al. 2018, Natur, 553, 182
Minter, A. H., Balser, D. S., & Kartaltepe, J. S. 2005, ApJ, 631, 376
Muller, C. A., & Oort, J. H. 1951, Natur, 168, 357
Ocker, S. K., & Cordes, J. M. 2024, RNAAS, 8, 17
Qian, L., Yao, R., Sun, J., et al. 2020, Innov, 1, 100053
Ranasinghe, S., Leahy, D. A., & Tian, W. 2018, OPhyJ, 4, 1
Reid, M. J., Menten, K. M., Brunthaler, A., et al. 2014, ApJ, 783, 130
Reid, M. J., Menten, K. M., Brunthaler, A., et al. 2019, ApJ, 885, 131
Schönrich, R., Binney, J., & Dehnen, W. 2010, MNRAS, 403, 1829
Seymour, A., Michilli, D., & Pleunis, Z., 2019 DM_phase: Algorithm for Correcting Dispersion of Radio Signals, Astrophysics Source Code Library, ascl:1910.004
Sieber, W., & Seiradakis, J. H. 1984, A&A, 130, 257
Stanimirović, S., Weisberg, J. M., Hedden, A., Devine, K. E., & Green, J. T. 2003, ApJL, 598, L23
Stanimirović, S., Weisberg, J. M., Pei, Z., Tuttle, K., & Green, J. T. 2010, ApJ, 720, 415
Stanimirović, S., & Zweibel, E. G. 2018, ARA&A, 56, 489
Taylor, J. H. 1992, RSPTA, 341, 117
Taylor, J. H., & Cordes, J. M. 1993, ApJ, 411, 674
Urquhart, J. S., Hoare, M. G., Lumsden, S. L., et al. 2012, MNRAS, 420, 1656
van de Hulst, H. C. 1945, NTvN, 11, 210
van Straten, W., & Bailes, M. 2011, PASA, 28, 1
Verbiest, J. P. W., Weisberg, J. M., Chael, A. A., Lee, K. J., & Lorimer, D. R. 2012, ApJ, 755, 39
Virtanen, P., Gommers, R., Oliphant, T. E., et al. 2020, NatMe, 17, 261
Wainscoat, R. J., Cohen, M., Volk, K., Walker, H. J., & Schwartz, D. E. 1992, ApJS, 83, 111
Weisberg, J. M., Rankin, J., & Boriakoff, V. 1980, A&A, 88, 84
Weisberg, J. M., & Stanimirović, S. 2007, in ASP Conf. Ser. 365, SINS - Small Ionized and Neutral Structures in the Diffuse Interstellar Medium, ed. M. Haverkorn & W. M. Goss (San Francisco, CA: ASP), 28
Weisberg, J. M., Stanimirović, S., Xilouris, K., et al. 2008, ApJ, 674, 286
Williams, D. R. W., & Davies, R. D. 1954, Natur, 173, 1182
Yao, J. M., Manchester, R. N., & Wang, N. 2017, ApJ, 835, 29